

# Integrated sensing and communication based on space-time-coding metasurfaces

Received: 14 May 2024

Accepted: 7 February 2025

Published online: 21 February 2025

 Check for updates

Xiao Qing Chen<sup>1,5</sup>, Lei Zhang<sup>1,5</sup>✉, Yi Ning Zheng<sup>1,5</sup>, Shuo Liu<sup>1</sup>,  
Zhuo Ran Huang<sup>1</sup>, Jing Cheng Liang<sup>1</sup>, Marco Di Renzo<sup>2,3</sup>✉, Vincenzo Galdi<sup>4</sup>✉ &  
Tie Jun Cui<sup>1</sup>✉

Programmable metasurfaces (PMs), also called reconfigurable intelligent surfaces (RISs), are planar structures capable of dynamically manipulating electromagnetic waves in real-time. Regarded as a key enabling technology for implementing smart wireless propagation environments, PMs/RISs also serve as an ideal supporting platform for integrated sensing and communication (ISAC). Here, we propose two ISAC schemes based on a special type of PMs/RISs: space-time-coding metasurfaces (STCMs). By leveraging space-time-coding strategies, STCMs simultaneously control the propagation at the fundamental (carrier) frequency for reliable wireless communication and generate spatially distributed harmonics for sensing. The proposed schemes seamlessly integrate both communication and sensing on a shared hardware platform, eliminating the need for additional sensors. For experimental validation, we implemented an ISAC system using a 2-bit STCM operating at microwave frequencies. Experimental results align with theoretical predictions, confirming the practical viability and effectiveness of the proposed ISAC schemes for applications in communication, imaging, radar, and sensing systems.

Programmable metasurfaces (PMs)<sup>1</sup>, which are also called reconfigurable intelligent surfaces (RISs)<sup>2–9</sup> in the communications community, are artificial planar structures that can dynamically control electromagnetic (EM) waves, reshaping the wavefronts and creating diverse scattering patterns. These advanced field-manipulation capabilities not only facilitate signal modulations but also enable communication and sensing systems to achieve adaptive and intelligent wireless environments<sup>1–9</sup>. Another emerging technology, known as integrated sensing and communication (ISAC), stands out as a prominent candidate for the sixth-generation (6G) of wireless communication systems, drawing considerable interest from researchers across different disciplines. In essence, ISAC aims to seamlessly integrate sensing and wireless communications by leveraging shared spectra, hardware

platforms, and signal processing functions. This integration seeks to achieve a balance in performance, while significantly reducing the hardware cost and power consumption<sup>10–18</sup>. The synergy between PM/RIS and ISAC systems holds promise for advancing the development of 6G wireless network technologies. Specifically, PMs/RISs not only contribute to enhancing and balancing multiple performance metrics in an ISAC system<sup>19–22</sup> but also possess inherent capabilities for autonomously integrating sensing and wireless communication functions<sup>23–26</sup>. The design of platforms that integrate communications and sensing functionalities is also considered an enabling technology to tackle some key challenges for the adoption of PMs/RISs in future wireless communication systems, which include channel estimation and the availability of power supply<sup>27,28</sup>. Given the interest in PM/RIS

<sup>1</sup>Institute of Electromagnetic Space and State Key Laboratory of Millimeter Waves, Southeast University, Nanjing, China. <sup>2</sup>Laboratoire des Signaux et Systèmes, Université Paris-Saclay, CNRS, CentraleSupélec, Gif-sur-Yvette, France. <sup>3</sup>Department of Engineering, King's College London, Centre for Telecommunications Research, London, UK. <sup>4</sup>Fields & Waves Lab, Department of Engineering, University of Sannio, Benevento, Italy. <sup>5</sup>These authors contributed equally: Xiao Qing Chen, Lei Zhang, Yi Ning Zheng. ✉ e-mail: [njzhanglei@seu.edu.cn](mailto:njzhanglei@seu.edu.cn); [marco.direnzo@universite-paris-saclay.fr](mailto:marco.direnzo@universite-paris-saclay.fr); [vgaldi@unisannio.it](mailto:vgaldi@unisannio.it); [tjcu@seu.edu.cn](mailto:tjcu@seu.edu.cn)

and ISAC in future communication networks, industry specification groups in pre-standardization organizations have been established as well (<https://www.etsi.org/committee/1966-ris>, <https://www.etsi.org/committee/2295-isac>). A recent overview on the synergy of PM/RIS and ISAC can be found in ref. 29.

PMs/RISs are two-dimensional versions of metamaterials. These artificial structures are composed of suitably designed sub-wavelength scattering units, and offer advantages in terms of ultra-low electrical thickness, resulting in higher integration, lower cost, and reduced insertion loss<sup>30–33</sup>. Through a careful design and arrangement of the scattering units, metasurfaces enable advanced control of EM wave properties, including amplitude, phase, and polarization. The concept of digital coding metasurfaces, initially introduced in 2014<sup>1</sup>, employs basic scattering units with a limited number of states that can be represented as discrete digits<sup>1,34</sup>. This digital approach makes coding metasurfaces ideal for integrating active devices, such as positive-intrinsic-negative (PIN) diodes, varactors, or tunable materials such as liquid crystals<sup>35,36</sup>. These tunable elements can be independently controlled by field programmable gate arrays (FPGA) to dynamically configure the EM responses of scattering units or supercells. This enables flexible and programmable real-time manipulations of EM waves, e.g., via a precise phase shift introduced by each scattering unit or supercell.

The advent of digital coding architectures not only streamlines the design and optimization process of metasurfaces but also empowers PMs to serve as versatile platforms for numerous applications, including reprogrammable holograms<sup>37,38</sup>, EM information theory<sup>39,40</sup>, reflect- and transmit-arrays<sup>41,42</sup>, vortex beam generations<sup>43</sup>, information processing<sup>44,45</sup>, wireless communications<sup>46–48</sup>, adaptive metasurfaces<sup>49</sup>, smart imaging<sup>50,51</sup>, and programmable artificial intelligence (AI) devices<sup>52</sup>. PMs/RISs offer a cost-effective, compact, lightweight, and low-power solution for integrating various functions. The integration of PMs/RISs into communication systems has been extensively researched, highlighting its significant advantages. Beyond communication, PMs/RISs can also be employed in sensing applications due to their cost-effective reconfigurability. When the direct path between the sensing target and a base station (BS) is obstructed, a PM/RIS can establish a non-line-of-sight link, reflecting signals to facilitate sensing operations<sup>19,20,53</sup>. In such a scenario, a PM/RIS cannot typically gather environmental sensing information on its own and usually relies on the BS to transmit external control signals via a dedicated control link for configuring its phase pattern. Alternatively, a PM/RIS can function as a physical sampling device by switching between multiple phase patterns. In this mode, it requires only a single receive channel to analyze the received signals from each phase pattern, thereby extracting sensing information<sup>24,50,54,55</sup>. However, in this configuration, it cannot simultaneously support communication functions. To address this limitation, sensors or detectors can be integrated into PMs/RISs to enable concurrent sensing and communication<sup>26,56,57</sup>. This allows for dynamic configuration of phase patterns, potentially eliminating the need for a dedicated control link from the BS. Nevertheless, this integration requires additional peripheral circuitry, leading to an increase in hardware costs.

Digital PMs/RISs conventionally operate with fixed space-coding (SC) patterns, controlled by a central module, to implement some desired functions for spatial beamforming. To manipulate the frequency spectra of EM waves, temporal encoding has gained attention, and the concept of space-time-coding (STC) digital metasurface has emerged as a rapidly growing research field<sup>58,59</sup>. This idea has found applications in various domains including programmable nonreciprocity<sup>60</sup>, harmonic controls<sup>61</sup>, spectrum camouflage<sup>62</sup>, sensing<sup>63–65</sup>, and wireless communications<sup>66,67</sup>. Through a suitable design and optimization of the STC matrix for spatio-temporal modulations, these platforms can effectively manipulate the EM waves in both spatial and frequency domains simultaneously.

In this context, we introduce a low-cost and efficient ISAC approach based on STC metasurfaces (STCMs), which can harness some specified harmonics for wireless sensing and can control the propagation of the fundamental frequency wave to establish reliable sensing and wireless communication links simultaneously on the same platform by controlling the STC matrix. To this end, we propose two coding strategies for STCM to simultaneously manipulate the fundamental-frequency wave and harmonics, which are referred to as “adjustable partitioning” and “full-aperture” schemes. Compared with conventional ISAC systems relying on phased array antennas, STCM-based ISAC systems offer advantages in terms of reduced hardware cost and power consumption. Moreover, leveraging the harmonics for sensing eliminates the need for additional sensors or a dedicated control link from the BS, enabling simultaneous execution of sensing and communication functions without interference.

## Results

### Principle of STCM-based communication and sensing

Referring to the concept illustrated in Fig. 1, the proposed scheme features an STCM that manipulates the incoming EM wave, controlling the direction of propagation of the fundamental frequency and simultaneously generating spatially distributed harmonics. The fundamental-frequency wave is used for communication, while the spatial-spectral characteristics of the harmonics are processed to accurately estimate the direction of arrival (DOA) of some targets. Using the DOA information, the STCM’s coding pattern is adjusted to ensure that the direction of the beam of the fundamental-frequency (carrier) wave is consistently steered towards the user’s location. This configuration allows the dual functions of wireless sensing and communication to operate simultaneously without mutual interference. Even changing the direction of the incoming waves, the STCM can continuously sense the DOA information in real time and can autonomously configure the corresponding coding pattern to establish a reliable communication link with the users, ensuring the required communication quality.

Without loss of generality, we consider a two-dimensional scenario featuring a 2-bit reflection-type STCM consisting of  $N$  columns of unit cells. Each unit cell provides four discrete operating states with relative reflection phases  $\{-\pi/2, 0, \pi/2, \pi\}$ , corresponding to the digits  $\{0, 1, 2, 3\}$ , respectively. Assuming identical reflection coefficients for all the unit cells in the  $n$ th-column, denoted as  $\Gamma_S^n$ , and considering a time-harmonic plane-wave illumination with suppressed time-dependence  $\exp(j2\pi f_c t)$  and an angle of incidence  $\theta_i$ , the far-field pattern at the fundamental frequency is expressed as

$$f_S(\theta, \theta_i) = f_e(\theta) \sum_{n=1}^N \Gamma_S^n \exp[jk_c d(n-1)(\sin \theta + \sin \theta_i)] \quad (1)$$

where  $f_e(\theta)$  denotes the scattering pattern of the unit cell at frequency  $f_c$ ,  $k_c = 2\pi f_c / c$  is the wavenumber in free space,  $c$  is the speed of light, and  $d$  is the spatial period of the unit cell. Given the angle of incidence  $\theta_i$  and the specified beam-pointing direction  $\theta_r^0$ , the phase response of the  $n$ th-column unit  $\Phi_n$  can be calculated in a systematic fashion, as detailed in Supplementary Note 1. This phase response is then quantized into discrete values and represented in the corresponding digital codes to generate the SC patterns (see Supplementary Note 1 for more details). Figure 2a shows a set of SC sequences for  $N=16$ , while the corresponding spatial scattering patterns (theoretically calculated for an angle of incidence  $\theta_i = 0^\circ$ ) are illustrated in Fig. 2b. In this example, the beam-pointing direction varies from  $-60^\circ$  to  $+60^\circ$  with a  $5^\circ$  step. It is evident that the STCM exhibits precise and flexible control over the beam-pointing direction.

When utilizing spatio-temporal modulation, the operating state of the  $n$ th-column of unit cells undergoes periodic changes according to a given time-coding sequence. The reflection coefficient of each

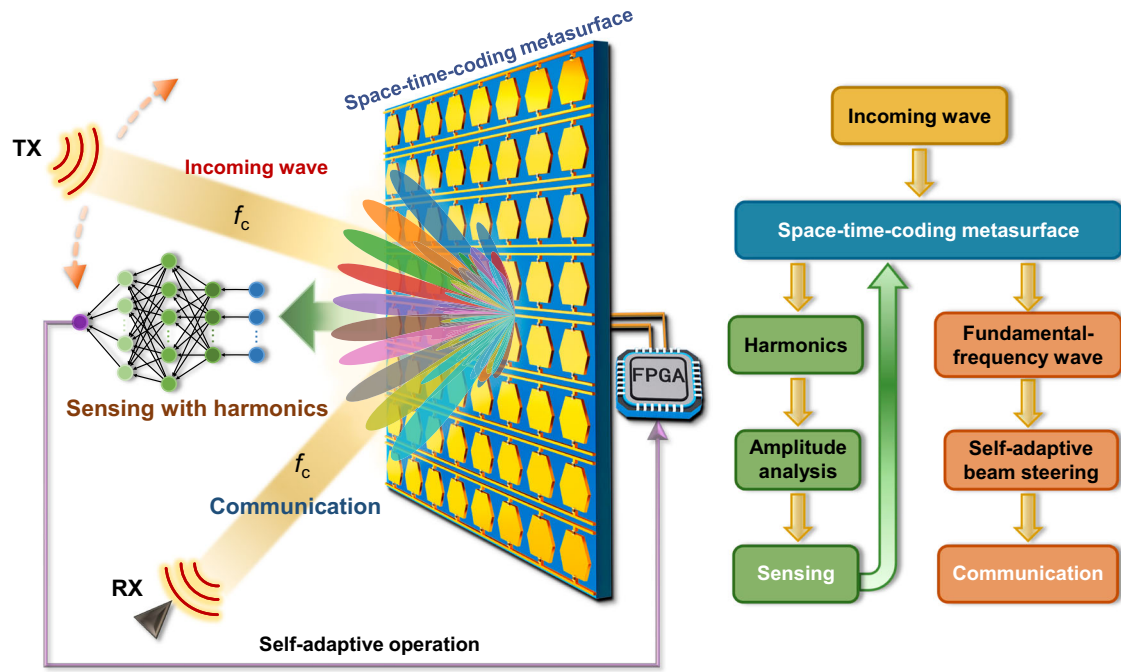


**Fig. 1 | Conceptual illustration of the proposed space-time-coding metasurface (STCM)-based integrated sensing and communication (ISAC) scheme.** in which an STCM controls the propagation direction of the fundamental-frequency wave for communication while generating spatially distributed harmonics for wireless sensing.

$n$ th-column of unit cells is represented by a periodic function  $\Gamma_T^n(t)$ <sup>58</sup>, which can be expanded into a Fourier series, with the generic coefficient expressed as  $a_\nu^n$ . The time-coding sequences of all  $N$  columns can be collectively represented as an STC matrix  $\mathbf{Z} \in \mathbf{R}^{N \times L}$ . Accordingly, for the assumed plane-wave illumination, the far-field scattering pattern at the  $\nu$ th harmonic frequency ( $f_c + \nu f_0$ ) (with  $f_0 = 1/T_0$  denoting the modulation frequency) is expressed in the slow-modulation limit ( $f_0 \ll f_c$ ) as<sup>58,59</sup>

$$f_T^\nu(\theta, \theta_i) = f_e(\theta) \sum_{n=1}^N a_\nu^n \exp(j(n-1)d[k_\nu \sin \theta + k_c \sin \theta_i]) \quad (2)$$

where  $k_\nu = 2\pi(f_c + \nu f_0)/c$  is the corresponding wavenumber (see Supplementary Note 2 for more details).

Via a suitable design of the STC matrix, we can modulate the spatial distribution of the harmonics while suppressing the fundamental-frequency component of the reflected wave. Figure 2c displays an optimized STC matrix with  $N = 16$  and  $L = 32$ , and the corresponding far-field harmonic scattering patterns (for  $\theta_i = 0^\circ$ ) are shown in Fig. 2d. It can be observed that the harmonics from the  $-5$ th to the  $+5$ th are uniformly distributed in space  $[-60^\circ, +60^\circ]$ , each pointing to a different direction, while the power of the fundamental-frequency wave is significantly suppressed (see Supplementary Note 3 for more details on the STC matrix optimization).

A STCM has the ability to simultaneously control the propagation of the fundamental-frequency wave and the spatial distribution of the harmonics. To achieve this, we define an STC matrix  $\mathbf{W}_T$ , which maintains a uniform duty cycle  $\tau_0$  across the unit cells of the  $N$ -column. Additionally, we introduce a time shift  $t_s$  between the  $n$ -th column and the  $(n+1)$ -th-column of unit cells, i.e.,  $\Gamma_T^{n+1}(t) = \Gamma_T^n(t - t_s)$ . Given the desired beam-pointing direction of the fundamental-frequency wave  $\theta_r^0$  and the angle of incidence  $\theta_i$ , the corresponding SC sequences can be represented as a time-invariant STC matrix  $\mathbf{W}_S$ . By combining (adding) the two STC matrices,  $\mathbf{W}_T$  and  $\mathbf{W}_S$ , we can obtain a new STC matrix. An example assuming  $N = 16$ ,  $\tau_0 = T_0/32$ ,  $t_s = T_0/16$ ,  $\theta_r^0 = -30^\circ$ , is shown in Fig. 2e and the corresponding far-field scattering patterns of the fundamental-frequency and harmonic waves are

presented in Fig. 2f. As can be observed, the obtained STC matrix effectively directs the fundamental-frequency wave to the desired angle  $\theta_r^0 = -30^\circ$  while generating multiple harmonics with distinct beam-pointing directions. Moreover, by adjusting the duty cycle  $\tau_0$  and the time shift  $t_s$ , the beam-pointing directions and powers of the harmonics can be finely tuned with the minimal impact on the beam-pointing direction of the fundamental-frequency wave. More details on the design of the STC matrix are provided in Supplementary Note 4.

By analyzing the spatial-spectral characteristics of the harmonics generated by the spatio-temporal modulation, the DOA information can be accurately estimated. Denoting as  $s_\nu(\theta_i) = |f_T^\nu(\theta = 0^\circ, \theta_i)|$  the scattered amplitudes at the harmonic frequencies  $f_c + \nu f_0$  ( $\nu = \pm 1, \pm 2 \dots \pm M$ ) along the normal direction, and arranging them into a vector  $\mathbf{s}(\theta_i)$  of dimension  $2M$ , we can define the corresponding normalized vector as  $\mathbf{x}(\theta_i) = \mathbf{s}(\theta_i) / \max[\mathbf{s}(\theta_i)]$ . The relationship between  $\mathbf{x}(\theta_i)$  and  $\theta_i$  can be exploited to estimate the direction of the incoming wave. Specifically, utilizing  $\mathbf{x}(\theta_i)$  as the input and  $\theta_i$  as the output, we train an artificial neural network (ANN) model to establish a robust and generalized mapping between them (see Supplementary Note 5 for details). Alternatively, this relationship can be characterized by constructing a sensing matrix for DOA estimation, as outlined in Supplementary Note 6. These DOA estimation methods rely solely on the amplitude of the harmonics, avoiding the use of phase information. This approach ensures low latency and is inherently suitable for in-situ estimation.

### STCM-based ISAC system

Considering the capability of STCM to manipulate the fundamental-frequency wave and harmonics, we propose two coding strategies for the STCM-based ISAC system, namely, the adjustable partitioning and full-aperture schemes. The adjustable partitioning scheme consists of partitioning the STCM by using different modulation strategies, as shown in Fig. 3a. The STCM is split into two regions: Region 1 performs spatio-temporal modulation, periodically switching its operating states according to the STC matrix, while Region 2 is configured with an SC pattern that can be switched on demand. Hence, the far-field pattern of the fundamental-frequency wave is the combination of the

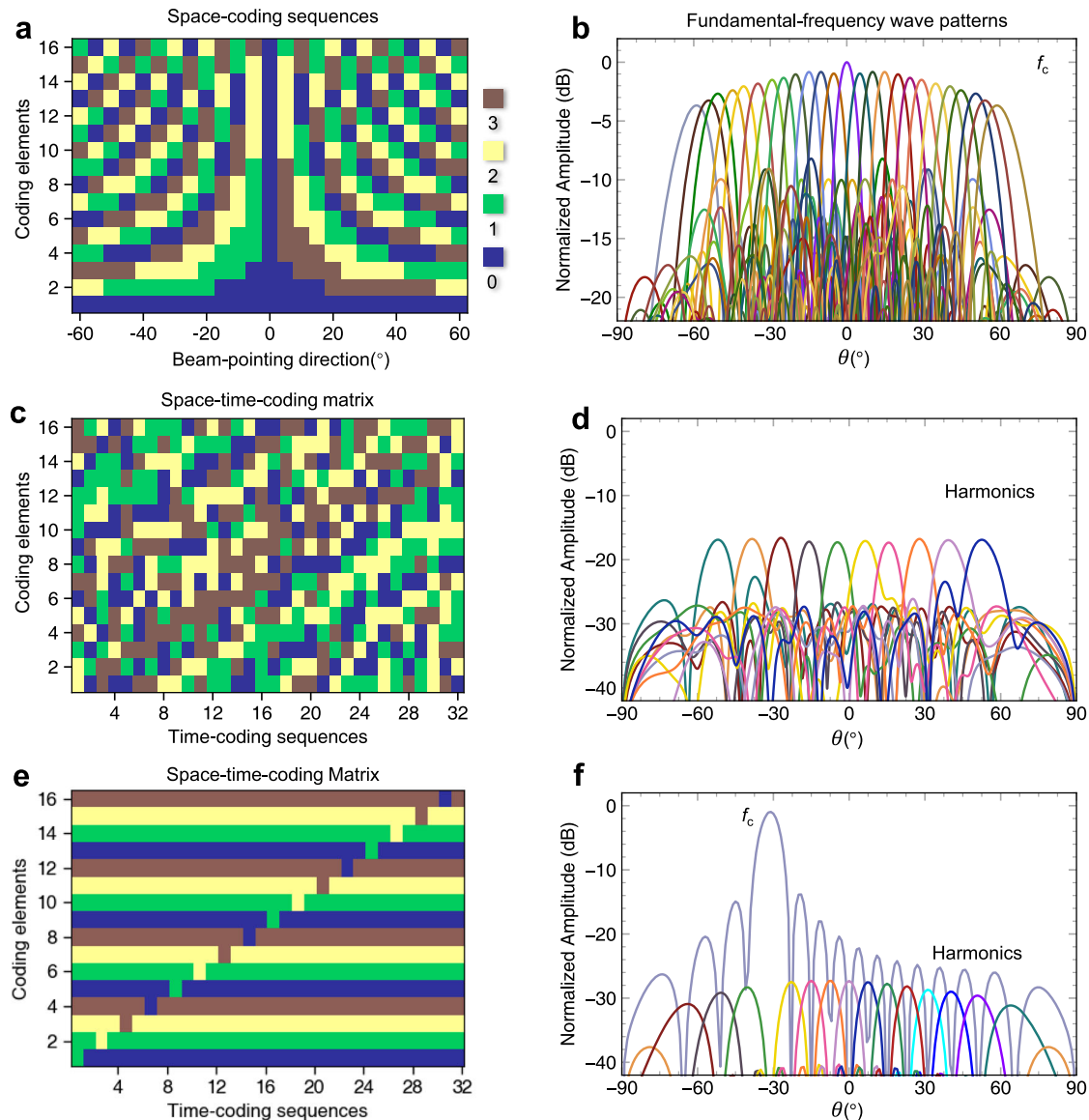


**Fig. 2 | Coding matrices and corresponding far-field scattering patterns of the proposed space-time-coding metasurface (STCM).** **a, b** Space-coding sequences for  $N=16$  and corresponding theoretical far-field patterns for the fundamental-frequency wave at  $\theta_i=0^\circ$ , respectively. **c, d** Optimized STC matrix for controlling

the harmonics when  $N=16$  and  $L=32$ , and corresponding far-field scattering patterns at  $\theta_i=0^\circ$ , respectively. **e, f** Optimized STC matrix for simultaneously controlling the fundamental-frequency wave and for generating multiple harmonics, and corresponding far-field scattering patterns, respectively.

far-field patterns of both regions. To reduce the interference with the beam shaping of the space-coding region of the STCM, it is essential to minimize the fundamental frequency component in the reflected wave of the spatio-temporal-modulated region. This approach enables the STCM to simultaneously optimize the fundamental-frequency wave and its harmonics, hence dynamically optimizing the power allocation between the communication and sensing by controlling the size of the two regions. Various power allocation strategies in ISAC systems have been extensively investigated under different optimization criteria<sup>68–70</sup>.

The full-aperture scheme for the STCM applies spatio-temporal modulation across the entire metasurface, as shown in Fig. 3b. Given the desired beam-pointing direction of the fundamental frequency wave  $\theta_r^0$ , the angle of incidence  $\theta_i$ , the duty cycle  $\tau_0$ , and the time shift  $t_s$ , the corresponding STC matrix can be generated (see the design flow in Supplementary Fig. 3). By designing the STC matrix, the propagation of the fundamental-frequency wave can be controlled for

communication while generating multiple harmonics with distinct spatial distributions for sensing. More details on this full-aperture coding strategy are provided in Supplementary Note 6.

Figure 3c illustrates the ISAC system architecture for simultaneous direction sensing and wireless communication. A commercial software-defined radio transceiver (NI USRP-2943R) is utilized for signal modulation and demodulation, by connecting each of its three ports to an antenna. Given that the operating frequency  $f_c$  of the STCM exceeds the upper bandwidth limit of the USRP, a mixer is integrated between the USRP port and the antenna. The modulated (finite-bandwidth) signal generated by the USRP undergoes up-conversion to frequency  $f_c$  before being transmitted via the antenna ANT1 to the STCM at an angle of incidence  $\theta_i$ . The incoming wave illuminating the spatio-temporal-modulated region of the STCM is converted into multiple harmonics and received by the antenna ANT2, which is positioned perpendicularly to the STCM. These received harmonics are down-converted to the frequency  $f_{IF}$  and are analyzed by the USRP.

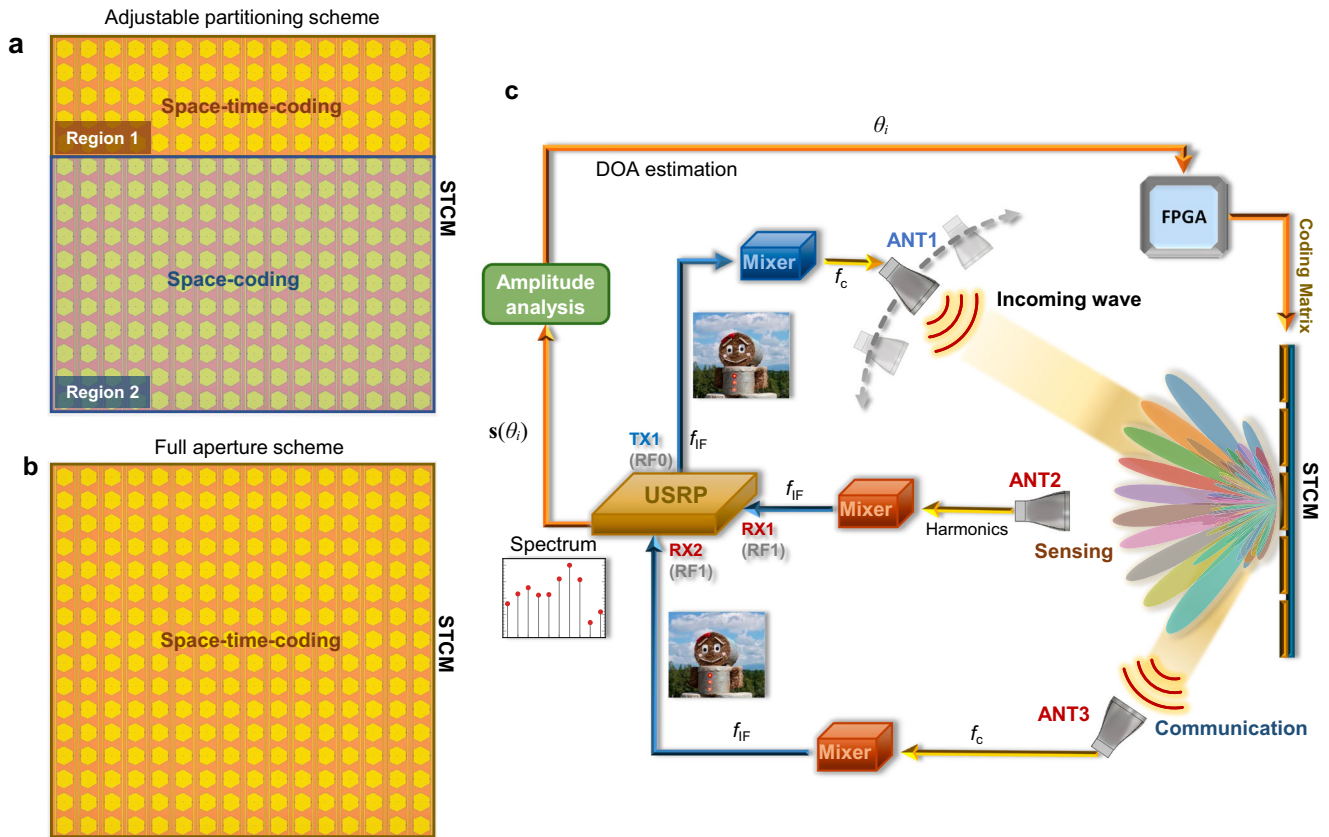


**Fig. 3 | Space-time-coding metasurface (STCM)-based integrated sensing and communication (ISAC) system architecture. a** Adjustable partitioning scheme of the STCM, which is divided into two regions for sensing and communication. The size of the two regions can be flexibly adjusted based on the required needs. **b** Full-aperture scheme of the STCM without partitioning, which can utilize the entire

STCM aperture by using STC matrices. **c** Architecture of the ISAC system, in which a USRP is used for signal modulation and demodulation, and the STCM establishes a reliable communication link by sensing the direction of the incoming wave in real-time and configuring the coding matrices.

By analyzing the amplitudes of the harmonics, the angle of incidence  $\theta_i$  of the incoming wave can be estimated. Based on this DOA information, the FPGA module adjusts the SC pattern of the STCM, so that the incoming wave is deflected to the direction  $\theta_r$ , is received by antenna ANT3, and is demodulated by the USRP to recover the signal. Any change in the position of ANT1 leads to a variation of the angle of incidence. Consequently, the amplitudes of the harmonics received by ANT2 are analyzed in real-time, and the coding pattern of the STCM is adjusted autonomously. This ensures the establishment of a reliable communication link between ANT1 and ANT3, irrespective of the angle of incidence  $\theta_i$ .

### Experimental verification and analysis

To assess the viability of the proposed approach, we fabricated a prototype of a 2-bit reflection-type STCM and tested its capability to manipulate the fundamental-frequency wave and the harmonics in a microwave anechoic chamber, as shown in Fig. 4a. The fabricated STCM prototype, operating at frequency  $f_c = 10.3$  GHz, comprises  $16 \times 16$  unit cells, and each unit cell is integrated with two PIN diodes (MACOM MADP-000907-14020x), as illustrated in Fig. 4b. The unit cells are designed such that a  $90^\circ$  phase difference is achieved when the two PIN diodes are switched among the four “OFF-OFF”, “ON-OFF”, “OFF-ON”, and “ON-ON” states, corresponding to the four digital states “0”, “1”, “2”, and “3”, respectively (see Supplementary Note 7 for more details).

We first measured the far-field scattering patterns of the fundamental-frequency wave and harmonics of the STCM, by utilizing

the coding strategy for the full-aperture scheme (see Supplementary Note 8 for more details). Assuming that  $\theta_r^0$  varies from  $-60^\circ$  to  $+60^\circ$  with a  $10^\circ$  increment and  $\theta_i = 0^\circ$ ,  $t_s = T_0/16$ ,  $\tau_0 = T_0/32$ , a series of STC matrices can be generated. In this case, the entire aperture of the STCM is exploited, relying only on STC matrices. The STCM is illuminated by a transmitting horn antenna with a monochromatic wave at 10.3 GHz, and the measured far-field scattering patterns of the fundamental frequency wave and the harmonics are shown in Fig. 4c. We also measured the far-field scattering patterns of the STCM with STC matrices for different values of the duty cycle  $\tau_0$  and time shift  $t_s$ . Assuming  $\theta_r^0 = 30^\circ$ , three matrices are generated, using the parameters  $t_s = T_0/16$ ,  $\tau_0 = T_0/32$ ;  $t_s = T_0/24$ ,  $\tau_0 = T_0/24$ ; and  $t_s = T_0/24$ ,  $\tau_0 = T_0/48$ , and the corresponding measured far-field scattering patterns are shown in Fig. 4d–f. The experimental results show the STCM capability of using the full-aperture scheme to manipulate the propagation of the fundamental-frequency wave and the spatial distribution of the harmonics. By analyzing the spatial-spectral characteristics of the harmonics, the DOA can be accurately estimated. Further details and experimental results for the full-aperture scheme are provided in Supplementary Note 6.

When the STCM is designed based on the adjustable partitioning scheme, two regions of the metasurface are configured with the SC patterns and the STC matrix, as shown in Fig. 2a and c, respectively. As an illustrative example, we consider that the STCM is divided into two regions of equal area, ensuring equal power allocation for wireless communication and sensing. The measured far-field scattering patterns of the fundamental-frequency wave are displayed in Fig. 5a.

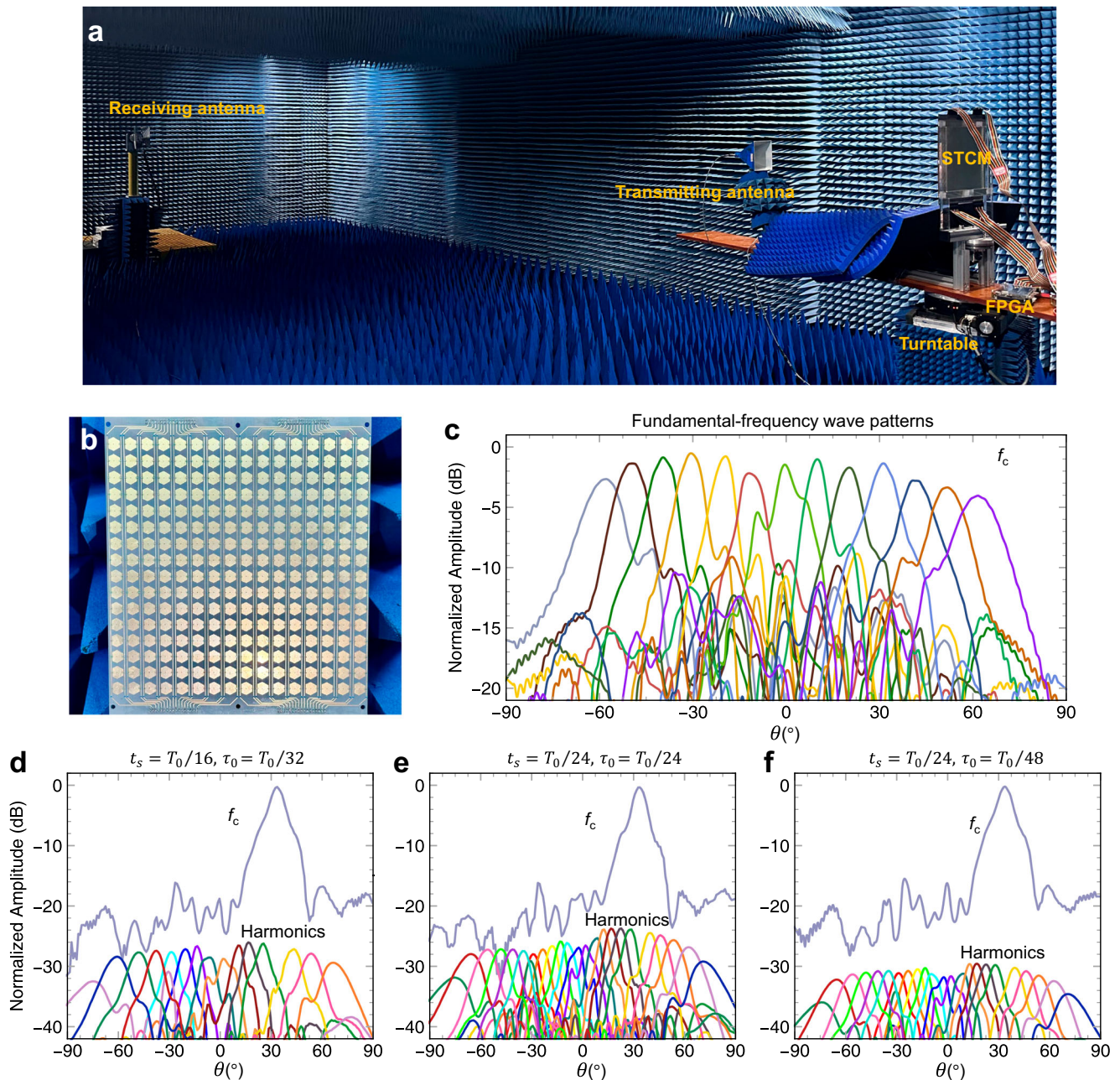


**Fig. 4 | Experimental validation of 2-bit space-time-coding metasurface (STCM) prototype and measured far-field patterns for the full-aperture scheme.**

**a** Measurement setup in an anechoic chamber. **b** Fabricated prototype of a 2-bit reflection-type STCM. **c**, Measured far-field scattering patterns of the fundamental-

frequency wave for different STC matrices as detailed in Supplementary Fig. 4a. **d–f**, Measured far-field scattering patterns corresponding to three STC matrices for different parameters of the duty cycle and time shift, as detailed in Supplementary Fig. 4d–f.

Figure 5b and c show the far-field harmonic scattering patterns (from the  $-5$ th to the  $+5$ th orders), with the reflected beams at the fundamental frequency pointing to the directions of  $-15^\circ$  and  $-30^\circ$  (corresponding to different space-coding patterns), respectively. We observe that these measurements closely resemble the simulation results in Fig. 2d. Additionally, the reflected power at the fundamental frequency (from Region 1 of the metasurface) is significantly suppressed, and different SC patterns have minimal impact on the spatial-spectrum characteristics of the harmonics. Moreover, the optimization of the direct-current (DC) voltage bias network on the STCM can enable the independent control of each unit cell, thereby enhancing

the flexibility in adjusting the area of each STCM region and the power distribution for communication and sensing, as illustrated in Supplementary Fig. 11. Further details on the optimization of the STCM can be found in Supplementary Note 9.

To generate the training data for the ANN model to perform DOA estimation, we measure the far-field harmonic scattering patterns under varying transmission powers and diode switching speeds. The trained model demonstrates high prediction accuracy on the test set across different transmission powers and diode switching speeds (see Supplementary Note 5 for details). In practical applications, the incoming wave is usually not monochromatic but carries a modulated

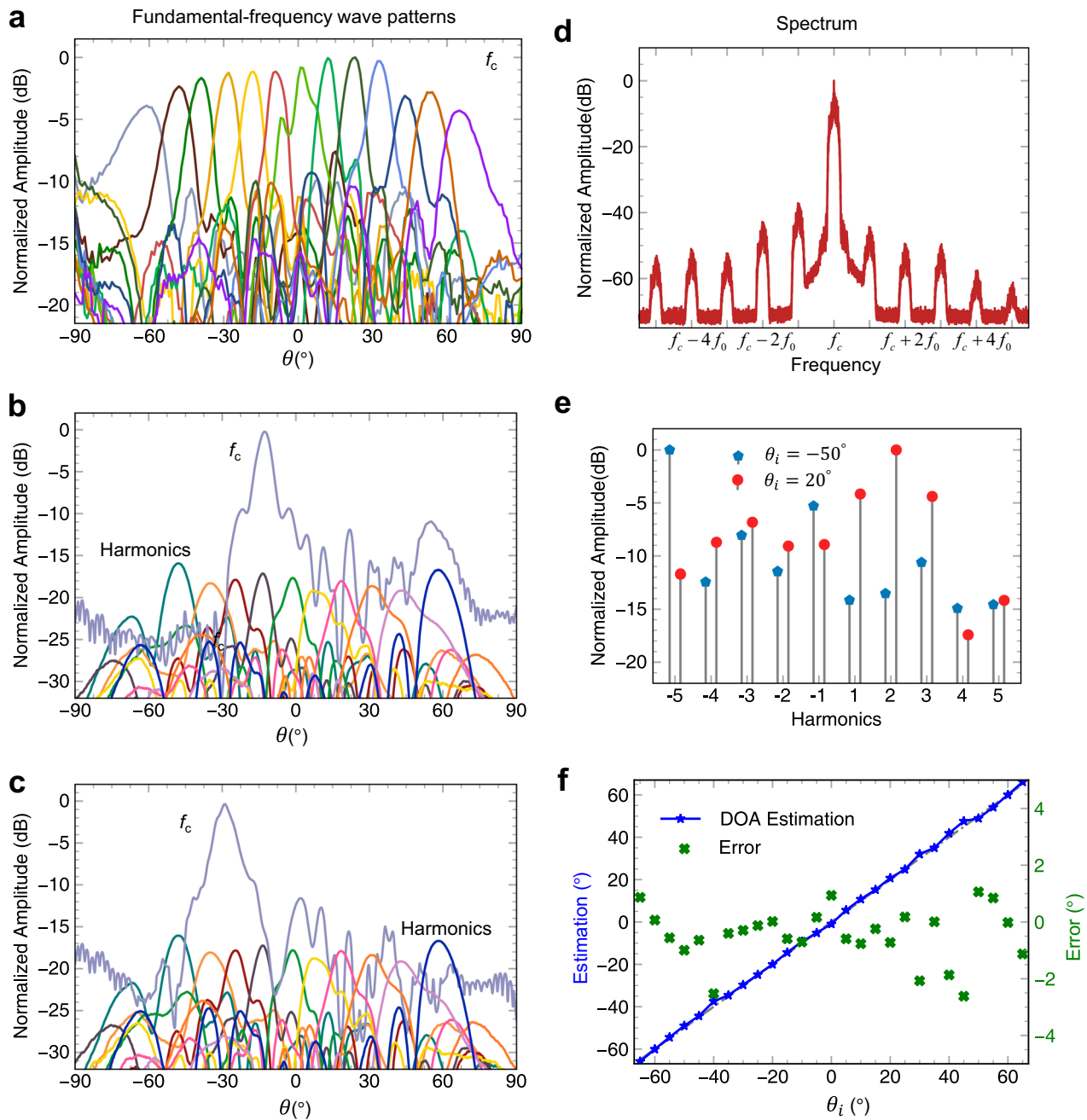


**Fig. 5 | Measured far-field patterns for the adjustable partitioning scheme and direction of arrival (DOA) estimation results using the artificial neural network (ANN) model. a** Measured far-field patterns of the fundamental-frequency wave for different SC sequences. **b, c** Measured far-field harmonic scattering patterns for the

reflected fundamental-frequency wave pointing to  $-15^\circ$  and  $-30^\circ$ , respectively. **d** Measured signal spectra received by antenna ANT2 (for  $\theta_i=0^\circ$ ). **e** Distribution of the normalized harmonic amplitude for  $\theta_i=-50^\circ$  and  $\theta_i=+20^\circ$ , respectively. **f** Results and errors for DOA estimation by using the ANN model.

finite-bandwidth signal. Hence, we further assess the performance of the ANN model by using a USRP-modulated signal, where a color image is encoded into a binary stream and modulated with a quadrature phase shift keying (QPSK) scheme. The modulated signal is up-converted to 10.3 GHz and transmitted through the antenna. Subsequently, after the STCM modulates the incoming wave, the generated harmonics are received and down-converted to the input port of the USRP for signal spectrum analysis. Here, the diode switching speed is set to 64 MHz, corresponding to a modulation frequency  $f_0=2$  MHz, and the symbol rate is 0.5 Mbps, while the angle of incidence  $\theta_i$  is

varied in the range  $[-65^\circ, +65^\circ]$  with a step of  $5^\circ$ . Then, the received signal spectrum corresponding to each angle of incidence is measured sequentially (see Supplementary Note 8 for more details). Figure 5d illustrates the received signal spectra for  $\theta_i=0^\circ$ , demonstrating no overlap between the signal spectra at the fundamental and harmonic frequencies. The signal spectra are normalized to form the input vector for the ANN model, as shown in Fig. 5e for  $\theta_i=-50^\circ$  and  $\theta_i=+20^\circ$ . The results and errors of the estimated DOA of the ANN model are presented in Fig. 5f, indicating that the DOA of the estimated angles is limited within  $3^\circ$ . Despite the fact that the ANN model

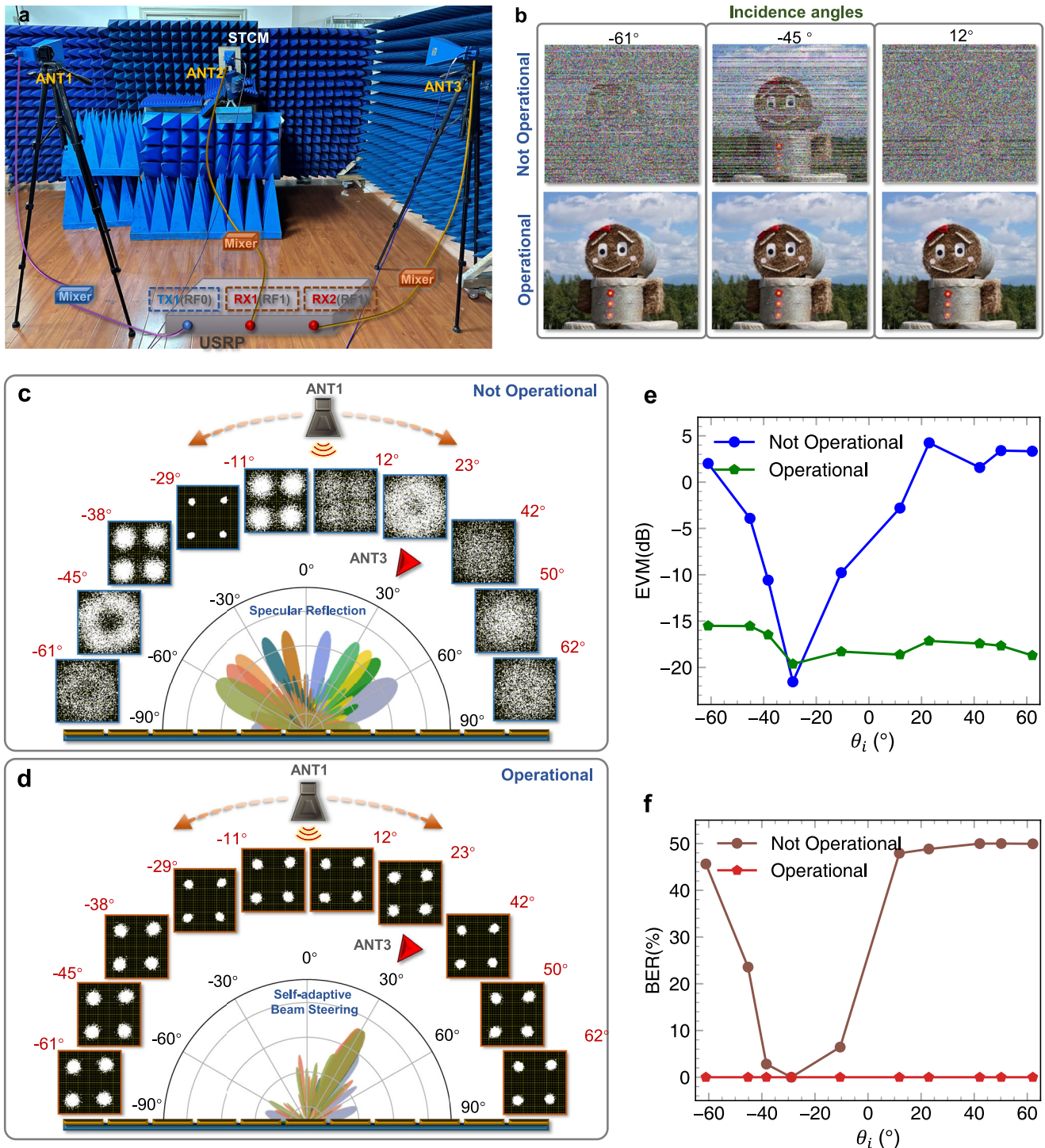


**Fig. 6 | Implementation and testing of the space-time-coding metasurface (STCM)-based integrated sensing and communication (ISAC) system.** **a** Experimental setup. **b** Received images corresponding to different angles of incidence when the STCM is not operational (upper panel) and operational (lower panel). **c–f** Measurement results for 10 positions of antenna ANT1. Demodulated

constellation diagrams when the STCM is not operational and operational, respectively. **e, f** Measured error vector magnitudes (EVMs), and bit error ratios (BERs), respectively, when the STCM is not operational and operational, for different angles of incidence.

is trained with a dataset for monochromatic incoming waves, the ANN architecture accurately estimates the angle of incidence even for finite-bandwidth modulated signals.

Subsequently, in line with the architecture in Fig. 3c, we implement the STCM-based system in an indoor setting to validate the proposed ISAC scheme, as illustrated in Fig. 6a. This proof-of-concept STCM-based ISAC system utilizes the adjustable partitioning scheme.

The signal generated by the USRP at the frequency of 1.5 GHz is up-converted to 10.3 GHz before illuminating the STCM via antenna ANT1. Antenna ANT2 is located in the normal direction to the STCM for receiving the harmonic signals, while antenna ANT3 is positioned at +30° for receiving the original modulated signal. The signals received by antennas ANT2 and ANT3 are down-converted to 1.5 GHz and are then sent to the two input ports (RX1(RF1) and RX2(RF1)) of the USRP

for analyzing the spectra of the harmonics and for demodulating the original signals, respectively. The position of antenna ANT1 varies across 10 selected measurement points, corresponding to the directions  $[-61^\circ, -45^\circ, -38^\circ, -29^\circ, -11^\circ, 12^\circ, 23^\circ, 42^\circ, 50^\circ, 62^\circ]$  based on the DOA estimation by the ANN architecture. Figure 6b illustrates three examples of different angles of incidence. When the STCM is operational, the space-coding pattern is determined based on the angle of incidence, hence ensuring that the reflected beam at the fundamental frequency points to the direction of antenna ANT3. Consequently, the original modulated signal can be successfully recovered. Conversely, when the STCM is inactive, the angle of incidence cannot be determined. As a result, the incoming wave is reflected to the specular direction with respect to antenna ANT1, leading to an incorrect data demodulation. Figure 6c–f shows the demodulated constellation diagrams, error vector magnitudes (EVMs), and bit error ratios (BERs) when the STCM is operational and not operational across the 10 antenna positions, respectively. Notably, when the STCM is inactive, the EVM remains relatively low only for angles of incidence very close to  $-30^\circ$  (i.e., specularly symmetrical with respect to antenna ANT3). However, deviations from  $-30^\circ$  result in the inability to recover the transmitted image, as it is apparent from the cluttered constellation diagrams and the increased EVM and BER. Conversely, when the STCM is operational, the demodulated constellation diagrams consistently exhibit good quality, and the EVM and BER are maintained at low levels, thus facilitating a satisfactory reconstruction of the transmitted image irrespective of the position of antenna ANT1. Hence, the STCM facilitates the establishment of reliable communication links between ANT1 and ANT3 by real-time sensing of the DOA. Further details can be found in Supplementary Note 10 and Supplementary Movie 1. We further validated the system's performance in real-world scenarios, including an outdoor environment and an indoor setting without absorbers, as detailed in Supplementary Note 11.

Moreover, although the scenario in Fig. 1 involves a single transmitter and requires the estimation of a single DOA, the proposed scheme is also capable of estimating the DOAs of multiple incoming signals (see Supplementary Note 6). Finally, it is also important to note that the proposed STCM-based ISAC scheme is not the only possible option. For instance, an alternative scheme utilizing the same platform is discussed in Supplementary Note 12, which is focused on establishing a fixed communication link and locating a passive target.

## Discussion

We have introduced a cost-effective and efficient ISAC scheme leveraging the STCM technology. The proposed approach operates by simultaneously controlling the fundamental-frequency and high-order harmonic waves, which enables the analysis of the spatial-spectral characteristics of the harmonics for DOA estimation while ensuring efficient communication through the fundamental-frequency wave. By leveraging the shared sensing information, this system enhances communication through beamforming, embodying the resource-sharing principles of ISAC. We have proposed two coding strategies based on the STCM technology and, with the aid of experiments, we have demonstrated their capability of precisely and flexibly shaping the fundamental-frequency wave and estimating the DOA, and dynamically adjusting the power allocation between the communication and sensing. Moreover, we have realized and tested an ISAC system based on the implemented STCM platform. The obtained experimental results have demonstrated real-time beam steering and DOA estimation capabilities. The proposed scheme offers several advantages, such as a simplified hardware architecture, the absence of additional sensors, and cost-effectiveness. These benefits significantly enhance the potential of STCMs and RISs, positioning them as pivotal technologies for future communication systems.

## Methods

### ANN implementation

The ANN model, illustrated in Supplementary Fig. 5a, consists of a 10-dimensional input layer, followed by four hidden layers with 128, 64, 32, and 16 neurons, respectively, and terminated by a 1-dimensional output layer. ReLU activation functions are employed across the ANN model, and the MSE is used as the loss function. This model is trained and optimized using TensorFlow<sup>71</sup> on a desktop computer equipped with an NVIDIA Quadro RTX 8000 Graphical Processing Unit (GPU), and an AMD Ryzen Threadripper 3970 × 32-Core Processor @3.69 GHz, and 256 GB of RAM, operating on Windows 10 (Microsoft). More details are available in Supplementary Note 5.

### Experimental setup of the USRP

The USRP is connected to a portable computer used for modulating and demodulating the data, analyzing the spectrum, and managing the USRP. The control software for the USRP is developed in LabVIEW 2023 from National Instruments (<https://www.ni.com/zh-cn/shop/labview.html>). For transmission, the USRP encodes a color image into a binary data stream, which is then segmented into data frames containing synchronization bits, frame order, and guard bits.

### Data availability

The data supporting the findings of this study are presented in the paper and in the Supplementary information or can be made available upon request by contacting the corresponding authors.

### Code availability

The customary computer codes utilized for this paper be made available upon request by contacting the corresponding authors.

## References

1. Cui, T. J., Qi, M. Q., Wan, X., Zhao, J. & Cheng, Q. Coding metamaterials, digital metamaterials and programmable metamaterials. *Light Sci. Appl.* **3**, e218 (2014).
2. Wu, Q. Q. & Zhang, R. Towards smart and reconfigurable environment: intelligent reflecting surface aided wireless network. *IEEE Commun. Mag.* **58**, 106–112 (2020).
3. Huang, C., Zappone, A., Alexandropoulos, G. C., Debbah, M. & Yuen, C. Reconfigurable intelligent surfaces for energy efficiency in wireless communication. *IEEE Trans. Wireless Commun.* **18**, 4157–4170 (2019).
4. Basar, E. et al. Wireless communications through reconfigurable intelligent surfaces. *IEEE Access* **7**, 116753–116773 (2019).
5. Di Renzo, M. et al. Smart radio environments empowered by reconfigurable intelligent surfaces: how it works, state of research, and the road ahead. *IEEE J. Sel. Areas Commun.* **38**, 2450–2525 (2020).
6. Dai, L. et al. Reconfigurable intelligent surface-based wireless communications: antenna design, prototyping, and experimental results. *IEEE Access* **8**, 45913–45923 (2020).
7. Di Renzo, M., Danufane, F. H. & Tretyakov, S. Communication models for reconfigurable intelligent surfaces: from surface electromagnetics to wireless networks optimization. *Proc. IEEE* **110**, 1164–1209 (2022).
8. Cheng, Q. et al. Reconfigurable intelligent surfaces: simplified-architecture transmitters—from theory to implementations. *Proc. IEEE* **110**, 1266–1289 (2022).
9. Lin, Z. et al. Refracting RIS-aided hybrid satellite-terrestrial relay networks: joint beamforming design and optimization. *IEEE Trans. Aerosp. Electron. Syst.* **58**, 3717–3724 (2022).
10. Saddik, G. N., Singh, R. S. & Brown, E. R. Ultra-wideband multi-functional communications/radar system. *IEEE Trans. Microwave Theory Tech.* **55**, 1431–1437 (2007).

11. Liu, Y., Liao, G., Xu, J., Yang, Z. & Zhang, Y. Adaptive OFDM integrated radar and communications waveform design based on information theory. *IEEE Commun. Lett.* **21**, 2174–2177 (2017).
12. Kumari, P., Choi, J., Gonzalez-Prelcic, N. & Heath, R. W. IEEE 802.11ad-based radar: an approach to joint vehicular communication-radar system. *IEEE Trans. Veh. Technol.* **67**, 3012–3027 (2018).
13. Hassanien, A., Amin, M. G., Aboutanios, E. & Himed, B. Dual-function radar communication systems: a solution to the spectrum congestion problem. *IEEE Signal Process. Mag.* **36**, 115–126 (2019).
14. Wang, X., Hassanien, A. & Amin, M. G. Dual-function MIMO radar communications system design via sparse array optimization. *IEEE Trans. Aerosp. Electron. Syst.* **55**, 1213–1226 (2019).
15. Liu, Y., Liao, G., Chen, Y., Xu, J. & Yin, Y. Super-resolution range and velocity estimations With OFDM integrated radar and communications waveform. *IEEE Trans. Veh. Technol.* **69**, 11659–11672 (2020).
16. Chiriyath, A. R., Paul, B. & Bliss, D. W. Radar-communications convergence: coexistence, cooperation, and co-design. *IEEE Trans. Cognit. Commun. Networking* **3**, 1–12 (2017).
17. Yuan, X. et al. Spatio-temporal power optimization for MIMO joint communication and radio sensing systems with training overhead. *IEEE Trans. Veh. Technol.* **70**, 514–528 (2021).
18. Liu, F., Masouros, C., Petropulu, A. P., Griffiths, H. & Hanzo, L. Joint radar and communication design: applications, state-of-the-art, and the road ahead. *IEEE Trans. Commun.* **68**, 3834–3862 (2020).
19. Chepuri, S. P. et al. Integrated sensing and communications with reconfigurable intelligent surfaces: from signal modeling to processing. *IEEE Signal Process. Mag.* **40**, 41–62 (2023).
20. Liu, R., Li, M., Liu, Y., Wu, Q. & Liu, Q. Joint transmit waveform and passive beamforming design for RIS-Aided DFRC systems. *IEEE J. Sel. Topics Signal Process.* **16**, 995–1010 (2022).
21. Xu, S. et al. Intelligent reflecting surface enabled integrated sensing, communication and computation. *IEEE Trans. Wireless Commun.* **23**, 2212–2225 (2023).
22. Xu, Y., Li, Y., Zhang, J. A., Renzo, M. D. & Quek, T. Q. S. Joint beamforming for RIS-assisted integrated sensing and communication systems. *IEEE Trans. Commun.* **72**, 2232–2246 (2024).
23. Zhang, H. et al. Holographic integrated sensing and communication. *IEEE J. Sel. Areas Commun.* **40**, 2114–2130 (2022).
24. Wan, X. et al. Information metasurface for electromagnetic sensing and wireless communications. *Adv. Mater. Technol.* **9**, 2301629 (2023).
25. Zhang, H., Zhang, H., Di, B. & Song, L. Holographic integrated sensing and communications: principles, technology, and implementation. *IEEE Commun. Mag.* **61**, 83–89 (2023).
26. Jiang, R. Z. et al. Simultaneously intelligent sensing and beamforming based on an adaptive information metasurface. *Adv. Sci.* **11**, 2306181 (2023).
27. Albanese, A., Devoti, F., Sciancalepore, V., Di Renzo, M. & Costa-Perez, X. MARISA: A self-configuring metasurfaces absorption and reflection solution towards 6G. *IEEE INFOCOM 2022*, 250–259 (2022).
28. Albanese, A., et al. ARES: Autonomous RIS solution with energy harvesting and self-configuration towards 6G. <https://arxiv.org/abs/2303.01161> (2023).
29. Magbool, A., Kumar, V., Wu, Q., Di Renzo, M. & Flanagan, M. F. A Survey on integrated sensing and communication with intelligent metasurfaces: trends, challenges, and opportunities. <https://arxiv.org/abs/2401.15562> (2024).
30. Yu, N. et al. Light propagation with phase discontinuities: generalized laws of reflection and refraction. *Science* **334**, 333–337 (2011).
31. Zheludev, N. I. & Kivshar, Y. S. From metamaterials to metadevices. *Nat. Mater.* **11**, 917–924 (2012).
32. Holloway, C. L. et al. An overview of the theory and applications of metasurfaces: the two-dimensional equivalents of metamaterials. *IEEE Antennas Propag. Mag.* **54**, 10–35 (2012).
33. Kildishev, A. V., Boltasseva, A. & Shalaev, V. M. Planar photonics with metasurfaces. *Science* **339**, 1232009 (2013).
34. Cui, T. J., Liu, S. & Zhang, L. Information metamaterials and metasurfaces. *J. Mater. Chem. C* **5**, 3644–3668 (2017).
35. Wang, L. et al. A review of THz modulators with dynamic tunable metasurfaces. *Nanomaterials* **9**, 965 (2019).
36. He, Q., Sun, S. & Zhou, L. Tunable/reconfigurable metasurfaces: physics and applications. *Research* **2019**, 1849272 (2019).
37. Li, L. et al. Electromagnetic reprogrammable coding-metasurface holograms. *Nat. Commun.* **8**, 197 (2017).
38. Venkatesh, S., Lu, X., Saeidi, H. & Sengupta, K. A high-speed programmable and scalable terahertz holographic metasurface based on tiled CMOS chips. *Nat. Electron.* **3**, 785–793 (2020).
39. Cui, T. J., Liu, S. & Li, L. L. Information entropy of coding metasurface. *Light: Sci. Appl.* **5**, e16172 (2016).
40. Wu, H. et al. Information theory of metasurfaces. *Natl. Sci. Rev.* **7**, 561–571 (2020).
41. Liu, S. et al. Anomalous refraction and nondiffractive bessel-beam generation of terahertz waves through transmission-type coding metasurfaces. *ACS Photonics* **3**, 1968–1977 (2016).
42. Zhang, L. et al. Transmission-reflection-integrated multifunctional coding metasurface for full-space controls of electromagnetic waves. *Adv. Funct. Mater.* **28**, 1802205 (2018).
43. Zhang, L., Liu, S., Li, L. L. & Cui, T. J. Spin-controlled multiple pencil beams and vortex beams with different polarizations generated by pancharatnam-berry coding metasurfaces. *ACS Appl. Mater. Interfaces* **9**, 36447–36455 (2017).
44. Cui, T. J. et al. Information metamaterials systems. *iScience* **23**, 101403 (2020).
45. Liu, S. et al. Convolution operations on coding metasurface to reach flexible and continuous controls of terahertz beams. *Adv. Sci.* **3**, 1600156 (2016).
46. Zhao, J. et al. Programmable time-domain digital-coding metasurface for non-linear harmonic manipulation and new wireless communication systems. *Natl. Sci. Rev.* **6**, 231–238 (2019).
47. Cui, T. J., Liu, S., Bai, G. D. & Ma, Q. Direct transmission of digital message via programmable coding metasurface. *Research* **2019**, 2584509 (2019).
48. Tang, W. et al. Wireless communications with programmable metasurface: new paradigms, opportunities, and challenges on transceiver design. *IEEE Wireless Commun.* **27**, 180–187 (2020).
49. Ma, Q. et al. Smart metasurface with self-adaptively reprogrammable functions. *Light: Sci. Appl.* **8**, 98 (2019).
50. Li, L. et al. Machine-learning reprogrammable metasurface imager. *Nat. Commun.* **10**, 1082 (2019).
51. Li, L. et al. Intelligent metasurface imager and recognizer. *Light Sci. Appl.* **8**, 97 (2019).
52. Liu, C. et al. A programmable diffractive deep neural network based on a digital-coding metasurface array. *Nat. Electron.* **5**, 113–122 (2022).
53. Liu, R. et al. Integrated sensing and communication with reconfigurable intelligent surfaces: opportunities, applications, and future directions. *IEEE Wireless Commun.* **30**, 50–57 (2023).
54. Hu, J. et al. Reconfigurable intelligent surface based RF sensing: design, optimization, and implementation. *IEEE J. Select. Areas Commun.* **38**, 2700–2716 (2020).
55. Lin, M. et al. Single sensor to estimate DOA with programmable metasurface. *IEEE Internet Things J.* **8**, 10187–10197 (2021).
56. Alexandropoulos, G. C. et al. Hybrid reconfigurable intelligent metasurfaces: enabling simultaneous tunable reflections and sensing for 6G wireless communications. *IEEE Veh. Technol. Mag.* **19**, 75–84 (2024).
57. Lin, Y., Jin, S., Matthaiou, M. & You, X. Tensor-based algebraic channel estimation for hybrid IRS-assisted MIMO-OFDM. *IEEE Trans. Wireless Commun.* **20**, 3770–3784 (2021).

58. Zhang, L. et al. Space-time-coding digital metasurfaces. *Nat. Commun.* **9**, 4334 (2018).
  59. Zhang, L. & Cui, T. J. Space-time-coding digital metasurfaces: principles and applications. *Research* **2021**, 9802673 (2021).
  60. Zhang, L. et al. Breaking reciprocity with space-time-coding digital metasurfaces. *Adv. Mater.* **31**, e1904069 (2019).
  61. Zhang, L. et al. Co-prime modulation for space-time-coding digital metasurfaces with ultralow-scattering characteristics. *Adv. Funct. Mater.* **34**, 2314110 (2024).
  62. Liu, M., Kozyrev, A. B. & Shadrivov, I. V. Time-varying metasurfaces for broadband spectral camouflage. *Phys. Rev. Appl.* **12**, 054052 (2019).
  63. Chen, X. Q., Zhang, L., Liu, S. & Cui, T. J. Artificial neural network for direction-of-arrival estimation and secure wireless communications via space-time-coding digital metasurfaces. *Adv. Opt. Mater.* **10**, 2201900 (2022).
  64. Fang, X. et al. Accurate direction-of-arrival estimation method based on space-time modulated metasurface. *IEEE Trans. Antennas Propag.* **70**, 10951–10964 (2022).
  65. Xia, D. et al. MetaBreath: multitarget respiration detection based on space-time-coding digital metasurface. *IEEE Trans. Microwave Theory Tech.* **72**, 1433–1443 (2023).
  66. Dai, J. Y. et al. Realization of multi-modulation schemes for wireless communication by time-domain digital coding metasurface. *IEEE Trans. Antennas Propag.* **68**, 1618–1627 (2020).
  67. Zhang, L. et al. A wireless communication scheme based on space- and frequency-division multiplexing using digital metasurfaces. *Nat. Electron.* **4**, 218–227 (2021).
  68. Behdad, Z., Demir, Ö. T., Sung, K. W., Björnson, E. & Cavdar, C. Multi-static target detection and power allocation for integrated sensing and communication in cell-free massive MIMO. *IEEE Trans. Wireless Commun.* **23**, 11580–11596 (2024).
  69. Pu, Z., Wang, W., Lao, Z., Yan, Y. & Qin, H. Power allocation of integrated sensing and communication system for the internet of vehicles. *IEEE Trans. Green Commun. Netw.* **8**, 1717–1728 (2024).
  70. Yang, H. et al. Dynamic power allocation for integrated sensing and communication-enabled vehicular networks. *IEEE Trans. Wireless Commun.* **23**, 12313–12330 (2024).
  71. Abadi, M., et al. TensorFlow: large-scale machine learning on heterogeneous distributed systems. <https://arxiv.org/abs/1603.04467> (2016).
- M.D.R), the Horizon Europe project UNITE under grant agreement number (101129618, M.D.R), the Horizon Europe project INSTINCT under grant agreement number (101139161, M.D.R), and the Horizon Europe project TWIN6G under grant agreement number (101182794, M.D.R), as well as by the Agence Nationale de la Recherche (ANR) through the France 2030 project ANR-PEPR Networks of the Future under grant agreement (NF-YACARI 22-PEFT-0005, M.D.R), and by the CHIST-ERA project PASSIONATE under grant agreements (CHIST-ERA-22-WAI-04, M.D.R, and ANR-23-CHR4-0003-01, M.D.R).

## Author contributions

T.J.C. and L.Z. suggested the designs, planned and supervised the work, in consultation with V.G. and M.D.R. L.Z. and X.Q.C. conceived the idea, carried out the analytical modeling and numerical simulations. L.Z., X.Q.C. and J.C.L. fabricated the prototype and performed the theoretical analysis. X.Q.C., L.Z. and Y.N.Z. built the system and performed the experimental measurements. X.Q.C., Z.R.H. and S.L. performed the data analysis. X.Q.C., L.Z., T.J.C., V.G., and M.D.R. wrote the manuscript. All authors discussed the theoretical aspects and numerical simulations, interpreted the results, and reviewed the manuscript.

## Competing interests

The authors declare no competing interests.

## Additional information

**Supplementary information** The online version contains supplementary material available at <https://doi.org/10.1038/s41467-025-57137-6>.

**Correspondence** and requests for materials should be addressed to Lei Zhang, Marco Di Renzo, Vincenzo Galdi or Tie Jun Cui.

**Peer review information** *Nature Communications* thanks Lingyang Song, Hongsheng Chen and the other anonymous reviewer(s) for their contribution to the peer review of this work. A peer review file is available.

**Reprints and permissions information** is available at <http://www.nature.com/reprints>

**Publisher's note** Springer Nature remains neutral with regard to jurisdictional claims in published maps and institutional affiliations.

**Open Access** This article is licensed under a Creative Commons Attribution-NonCommercial-NoDerivatives 4.0 International License, which permits any non-commercial use, sharing, distribution and reproduction in any medium or format, as long as you give appropriate credit to the original author(s) and the source, provide a link to the Creative Commons licence, and indicate if you modified the licensed material. You do not have permission under this licence to share adapted material derived from this article or parts of it. The images or other third party material in this article are included in the article's Creative Commons licence, unless indicated otherwise in a credit line to the material. If material is not included in the article's Creative Commons licence and your intended use is not permitted by statutory regulation or exceeds the permitted use, you will need to obtain permission directly from the copyright holder. To view a copy of this licence, visit <http://creativecommons.org/licenses/by-nc-nd/4.0/>.

© The Author(s) 2025

## Acknowledgements

This work was supported by the National Key Research and Development Program of China (2023YFB3811504, S.L.), the National Natural Science Foundation of China (62288101, T.J.C., 62101123, L.Z., U22A2001, S.L., and 62201136, S.L.), the Jiangsu Province Frontier Leading Technology Basic Research Project (BK20212002, T.J.C.), the Fundamental Research Funds for the Central Universities (2242023K5002, L.Z.), the 111 Project (111-2-05, T.J.C.), the National Postdoctoral Program for Innovative Talents (BX2021062, L.Z.), the Young Elite Scientists Sponsorship Program by CAST (2020QNR001, L.Z.), the China Postdoctoral Science Foundation (2020M680062, L.Z.), and the Jiangsu Planned Projects for Postdoctoral Research Funds (2021K058A, L.Z.). The work of V.G. was partially supported by the European Union under the Italian National Recovery and Resilience Plan (NRRP) of NextGenerationEU, partnership on “Telecommunications of the Future” (PE00000001 - program “RESTART”, V.G.). The work of M.D.R. was supported in part by the European Union through the Horizon Europe project COVER under grant agreement number (101086228,